Hierarchically heterostructured metal hydr(oxy)oxides for efficient overall water splitting†

Yang Liu,‡[a,b] Fengmei Wang,‡[a] Tofik Ahmed Shifa,[a] Jie Li,[a,b] Jing Tai,[c] Yu Zhang,[a] Junwei Chu,[a] Xueying Zhan,[a] Chongxin Shan*[d] and Jun He [ID] *[a,b]

The design of highly efficient electrocatalysts containing non-precious metals is crucial for promoting overall water splitting in alkaline media. In particular, Janus catalysts simultaneously facilitating the hydrogen evolution reaction (HER) and oxygen evolution reaction (OER) are desirable. Herein, we fabricated a unique hierarchical heterostructure *via* growing $Ni_4W_6O_{21}(OH)_2 \cdot 4H_2O$ (denoted as Ni−W−O) nanosheets on $NiMoO_4$ rods, which was indispensable for regulating the morphology of the Ni−W−O structure. This heterostructure of Ni−W−O/NiMoO_4 could be utilized as an electrocatalyst to realize superior activity for overall water splitting in 1.0 M KOH. It substantially promoted overall water splitting with 1.6 V at 30 mA cm^{-2}, outperforming numerous bifunctional electrocatalysts under the same conditions. Notably, the remarkable stability for continuously splitting water endowed this hierarchical heterostructure with potential applications on a large scale. This work emphasizes the effectively controlled growth of heterostructured non-noble-metal catalysts for energy-conversion reaction.

Introduction

Electrochemical water splitting, involving the hydrogen reaction (HER) and oxygen evolution reaction (OER), is one of the most promising technologies to alleviate the environmental crisis.[1,2] Platinum (Pt)- and iridium (Ir)- or ruthenium (Ru)-based oxides are acknowledged as superior catalysts for HER and OER, respectively.[3,4] However, their scarcity and high cost hinder their industrial applications to practically solve the current global energy problem. In water splitting reactions, OER is kinetically sluggish and thermodynamically challenging as compared to HER. Remarkable development[5–7] has been made so far in regard to promising catalysts for HER in acidic electrolytes. It is also true that OER occurs more easily in an alkaline electrolyte than in an acidic electrolyte.[8,9] Therefore, efforts are being devoted to the rational design of novel electrocatalysts that simultaneously catalyze both HER and OER under the same conditions. For instance, FeCoNi ternary alloys encapsulated in graphene layers can tune the electronic structures of materials to exhibit superior catalytic performances.[10] Also, Cu nanowires grown on few-layer NiFe layered double hydroxide (LDH) nanosheets provide high surface areas, fast electron transport, and open channels for effective gas release, effectively improving the overall water splitting performance.[11] Notably, metal (hydr)oxides containing Ni atoms, *e.g.*, Ni–Mo oxides,[12–15] Ni–Co oxides,[16,17] and Ni–Fe layered double hydroxides[18] have been intensively explored to generate oxygen gas in alkaline media. The adsorption energy of hydroxyl ions on Ni-based hydr(oxy)oxide can be easily tuned by introducing other metal atoms.[19,20] Meanwhile, nickel (Ni) atoms can act as water dissociation centers when combined with other transition metal atoms, especially Mo atoms.[21,22] This suggests that binary Ni- and Mo-based oxides are prospective candidates for splitting water. However, there are only a few studies about the OER catalytic activity of Ni–Mo oxides.

Here, we fabricated a hierarchical heterostructure of $Ni_4W_6O_{21}(OH)_2 \cdot 4H_2O$ nanosheets grown on $NiMoO_4$ rods (denoted as Ni–W–O/NiMoO_4). There were some remarkable advantages of fabricating this type of hierarchical heterostructure. First, the $NiMoO_4$ micro-structure not only provided

[a]*CAS Center for Excellence in Nanoscience, CAS Key Laboratory of Nanosystem and Hierarchical Fabrication, National Center for Nanoscience and Technology, Beijing 100190, China. E-mail: hej@nanoctr.cn*
[b]*Center of Materials Science and Optoelectronics Engineering, University of Chinese Academy of Sciences, Beijing 100049, P. R. China*
[c]*Testing and Analysis Center, Institute of Chemistry, Chinese Academy of Sciences, Beijing 100190, China*
[d]*School of Physics and Engineering, Zhengzhou University, Zhengzhou 450001, China. E-mail: cxshan@zzu.edu.cn*
†Electronic supplementary information (ESI) available. See DOI: 10.1039/c9nr02988e
‡These authors contributed equally.

a high surface area but also boosted the HER and OER activities by increasing the release of H_2 and O_2 bubbles from the surface of the electrode.[23] Second, the two types of Ni-based materials Ni–W–O and $NiMoO_4$ could effectively promote water dissociation on their surface due to the existence of Ni atoms. Furthermore, the effective interaction between Ni–W–O and $NiMoO_4$ could regulate the electronic structure of the electrocatalyst for synergistically improving the HER and OER activities. The hierarchical Ni–W–O/$NiMoO_4$ on a conductive Ni foam was synthesized *via* a two-step hydrothermal method. In particular, the $NiMoO_4$ rod played a crucial role in the realization of Ni–W–O nanosheets. The electronic coupling on the interface between Ni–W–O and $NiMoO_4$ endowed our novel material with bifunctional electrocatalytic activity in 1.0 M KOH. In HER, the synthesized hierarchical Ni–W–O/$NiMoO_4$ electrode showed a low overpotential of ∼52 mV, which was close to the value obtained using a Pt foil under the same conditions at a current density of 10 mA cm^{-2}. The Tafel slope of 80 mV dec^{-1}, which was much lower than those of $NiMoO_4$ (95 mV dec^{-1}) and pure Ni–W–O (131 mV dec^{-1}), was also recorded for the Ni–W–O/$NiMoO_4$ electrode. Moreover, this heterostructure exhibited a superior OER performance with an overpotential of 253 mV at 30 mA cm^{-2} and a Tafel slope of 92 mV dec^{-1}. The observed superior stability, withstanding continuous measurements in 1.0 M KOH for more than 3 days, further demonstrated its potential for industrial utilization. As expected, overall water splitting based on the Ni–W–O/$NiMoO_4$ heterostructure was realized under a low voltage of 1.6 V at a current density of 30 mA cm^{-2}. Our results offer a paradigm for establishing a platform for synergistic catalysis.

Results and discussion

Hierarchical Ni–W–O/$NiMoO_4$ heterostructures were prepared on a porous Ni foam (NF, Fig. S1a†) through a simple two-step hydrothermal method, and they exhibited sufficient mechanical strength and conductivity, as illustrated in Fig. 1a. This yielded hierarchically assembled Ni–W–O nanosheets onto the $NiMoO_4$ rods (denoted as Ni–W–O/$NiMoO_4$). The concentrations of the precursors such as $NiCl_2 \cdot 6H_2O$ and $(NH_4)_{10}W_{12}O_{41} \cdot xH_2O$ played a significant role in tuning the morphology of the as-grown material on the $NiMoO_4$ rods. Hence, we made careful optimization to obtain nanosheet morphology for superior electrocatalysis. To this end, the desired morphology of the Ni–W–O nanostructure on $NiMoO_4$ rods was obtained with the concentrations of 0.033 mol L^{-1} for $NiCl_2 \cdot 6H_2O$ and 0.033 mol L^{-1} for $(NH_4)_{10}W_{12}O_{41} \cdot xH_2O$. Accordingly, the as-prepared heterostructure is defined as "Ni–W–O/$NiMoO_4$-1". For comparison, a heterostructure (Ni–W–O/$NiMoO_4$-2) with increased concentrations of $NiCl_2 \cdot 6H_2O$ (0.066 mol L^{-1}) and $(NH_4)_{10}W_{12}O_{41} \cdot xH_2O$ (0.066 mol L^{-1}) was also prepared. From the scanning electron microscopy (SEM) image in Fig. S1b,† it can be seen that the diameter and length of each $NiMoO_4$ rod are around 400–500 nm and 20–30 μm, respectively, and it is capable of hosting the incoming nanosheet. The energy dispersive X-ray spectrum (EDX, Fig. S1c†) reveals the existence of Mo, Ni and O elements in the formed $NiMoO_4$. Meanwhile, the X-ray diffraction pattern (XRD, Fig. S2†) of the as-synthesized $NiMoO_4$ crystals demonstrates the typical diffraction peaks located at 14.3°, 28.9° and 32.6°, which are well identified as the (110), (220) and (022)
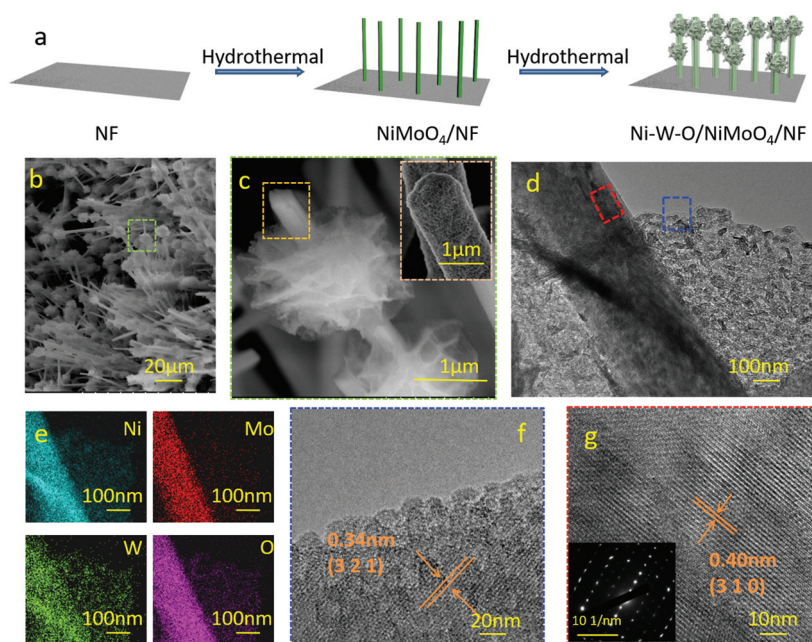

Fig. 1 (a) Schematic diagram of the synthesis of the Ni–W–O/$NiMoO_4$-1 heterostructure. (b–c) SEM images of Ni–W–O/$NiMoO_4$-1 heterostructure under different magnifications. The inset in c: the part marked with orange line. TEM image (d), EDX mapping (e), and HRTEM images (f–g) of the heterostructure. Inset in g: the SAED patterns marked in d.

planes of the monoclinic $NiMoO_4$ phase, respectively (PDF#33-0948). The other diffraction peaks at 44.5°, 51.9° and 76.1° are assigned to the Ni foam. The SEM images of the Ni–W–O/$NiMoO_4$-1 arrays under different magnifications are shown in Fig. 1b and c. The size of the obtained microstructures along with the nanosheets was about 2 μm and the diameter of the rods further increased to 1 μm (the inset of Fig. 1c). As shown in Fig. 1d, the transmission electron microscopy (TEM) image of Ni–W–O/$NiMoO_4$-1 further displays that the Ni–W–O nanosheets uniformly cover the surface of the $NiMoO_4$ rods. This corroborates the achievement of a unique hierarchical heterostructure. Also, the EDX mapping of an Ni–W–O/$NiMoO_4$-1 microrod (Fig. 1e) exhibits the uniform distribution of the Ni, Mo, W and O elements throughout the microrod. The lattice fringes with interplanar distances of 0.34 and 0.4 nm in the high-resolution TEM images (HRTEM, Fig. 1f and g) of the nanosheet can be indexed to the (321) and (310) planes of the $Ni_4W_6O_{21}(OH)_2 \cdot 4H_2O$ crystal (PDF#47-0143), respectively. Moreover, the selected area electron diffraction (SAED, inset of Fig. 1g) pattern also demonstrates its high crystallinity. As the concentration of $NiCl_2 \cdot 6H_2O$ and $(NH_4)_{10}W_{12}O_{41} \cdot xH_2O$ doubled (0.066 mol L^{-1}), the morphology of Ni–W–O/$NiMoO_4$-2 changed accordingly. Its SEM image (Fig. S3†) shows that microcubes instead of sheets with a size of around 4–5 μm assemble at the rods. Meanwhile, from the XRD pattern, XPS spectra and TEM images of Ni–W–O/$NiMoO_4$-2 in Fig. S4–6,† we can see that there is no obvious difference in the crystal phase and the components. For revealing the growth mechanism in this process, an intermediate sample (Ni–W–O/$NiMoO_4$-1.5) was also synthesized using a moderate concentration (0.05 mol L^{-1}) of $NiCl_2 \cdot 6H_2O$ and $(NH_4)_{10}W_{12}O_{41} \cdot xH_2O$. From the SEM image in Fig. S7,† we infer that the sheets on the $NiMoO_4$ rods consist of particles and demonstrate high thickness. This result indicates that the

concentration of the precursor plays a key role in controlling the morphology of the heterostructure. A low concentration is beneficial for the growth of thin Ni–W–O nanosheets due to the slow reaction rate. We also tried the experiment without the $NiMoO_4$ rods to practically determine the role of the first growth step in tuning the morphology of the hierarchical heterostructure. Fig. S8† shows that the obtained Ni–W–O structure grown directly on a Ni foam appears as microcubes; this is significantly different from the case where there is $NiMoO_4$ prior to the growth of Ni–W–O nanosheets. This result reveals that the $NiMoO_4$ rods are essential for directing the growth of Ni–W–O into nanosheet morphology.

In order to further characterize the components of the Ni–W–O/$NiMoO_4$-1 heterostructure, the XRD pattern was obtained (Fig. 2a). Compared with the XRD pattern of pure $NiMoO_4$ rods on a Ni foam, new diffraction peaks at 9.7°, 16.9°, 31.2°, etc. emerged for the Ni–W–O/$NiMoO_4$-1 arrays, demonstrating the existence of the cubic $Ni_4W_6O_{21}(OH)_2 \cdot 4H_2O$ phase (PDF#47-0143). Moreover, the X-ray photoelectron spectra (XPS, Fig. 2b and Fig. S9†) of various samples were recorded for studying the electronic structure of the heterostructure. The Ni $2p_{3/2}$ and $2p_{1/2}$ peaks of $NiMoO_4$ (Fig. 2c) are located at 856.60 and 874.37 eV, respectively, along with two satellite peaks at 862.40 and 880.19 eV.[24,25] It should be noted that there was a shift of 0.6 eV to lower binding energies (856.0 eV and 873.8 eV for Ni $2p_{3/2}$ and $2p_{1/2}$, respectively) for Ni–W–O/$NiMoO_4$-1 compared to that for pure $NiMoO_4$. This revealed the regulation of the electronic structure after the construction of the Ni–W–O/$NiMoO_4$ heterostructure. Fig. 2d demonstrates the deconvolution analysis of the Mo 3d bonding modes in various samples. For the $NiMoO_4$ rods, the peaks at binding energies of 232.20 eV and 235.25 eV corresponding to Mo $3d_{5/2}$ and Mo $3d_{3/2}$ are in agreement with the previously reported values for the Mo^{6+} oxidation state.[24] After growing Ni–W–O nanosheets, the
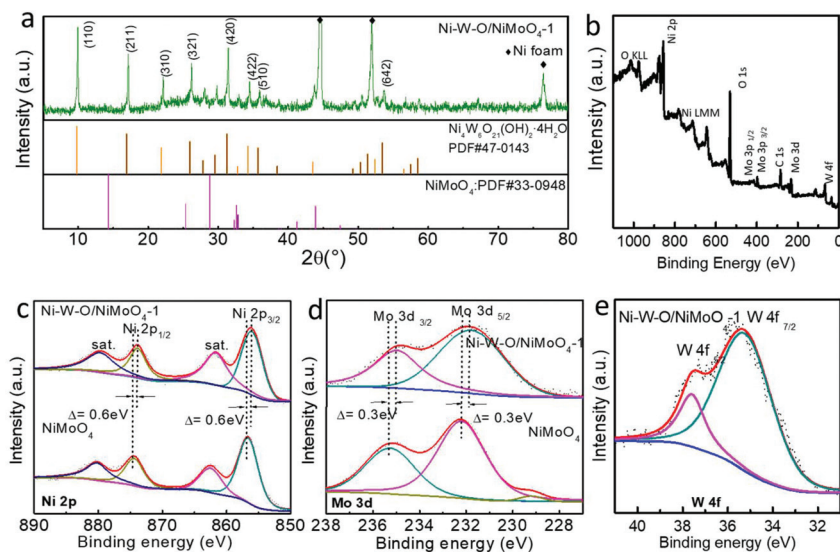

Fig. 2 (a) XRD pattern, XPS analysis of survey scan (b), Ni 2p (c), Mo 3d (d) and W 2f (e) spectra for the obtained Ni–W–O/$NiMoO_4$-1 heterostructure.

Mo $3d_{5/2}$ peak shifted by 0.3 eV to a lower binding energy, verifying that charge redistribution occurred on the interface. The two peaks situated at 35.23 and 37.6 eV in the W 4f region are assigned to W $4f_{7/2}$ and W $4f_{5/2}$ of W^{6+}, respectively (Fig. 2e).[26] This result suggests that the W element in the heterostructure can possibly act as electron-donating sites to tune the electronic structure of $NiMoO_4$.

The electrocatalytic activities of various samples were evaluated in 1.0 M KOH. A typical three-electrode setup with an Hg/HgO electrode and a glass carbon plate as the reference and counter electrodes, respectively, was utilized here. Ni–W–O/NiMoO₄-1 acted as the working electrode. For comparison, the pure NiMoO₄, Ni–W–O, and Ni–W–O/NiMoO₄-2 electrodes were also measured under the same conditions. Their HER activities were investigated in N_2 gas (99.99%)-saturated 1.0 M KOH. The polarization curves shown in Fig. 3a display the superior HER performance of the Ni–W–O/NiMoO₄-1 electrode with an overpotential (η_{10}) of ~52 mV, which is much smaller than those of the Ni–W–O/NiMoO₄-2 (~100 mV), NiMoO₄ (~234 mV), and Ni–W–O (258 mV) electrodes at 10 mA cm^{-2}. Importantly, the catalytic activity of Ni–W–O/NiMoO₄-1 was comparable to that of a pure Pt foil (30 mV at 10 mA cm^{-2}). Thus, the growth of the Ni–W–O nanosheets on the surface of NiMoO₄ endowed a highly enhanced performance for the heterostructure due to its optimum morphology and synergistic effect. The η_{10} values of various electrodes shown in Fig. 3b obviously demonstrate the outstanding performance of the Ni–W–O/NiMoO₄-1 heterostructure (Table S1†). The corresponding Tafel plots are shown in Fig. 3c. As expected, the Tafel slope of Ni–W–O/NiMoO₄-1 is

80 mV dec^{-1}, which is much lower than those of the Ni–W–O/NiMoO₄-2 (158 mV dec^{-1}), NiMoO₄ (95 mV dec^{-1}) and pure Ni–W–O (131 mV dec^{-1}) electrodes. The higher Tafel slopes of the Ni–W–O/NiMoO₄-2 and Ni–W–O electrodes indicated that the microcube morphology of Ni–W–O hindered the adsorption of H_2O molecules ($H_2O + M + e^- \rightarrow M^-H^* + OH^-$, where M denotes the electrocatalyst) on the surface. As an important descriptor to evaluate the kinetics of electrocatalysts, we measured the exchange current density (j_0) and found a value of 4.615 mA cm^{-2} for the Ni–W–O/NiMoO₄-1 electrode, which outperformed the Ni–W–O/NiMoO₄-2 (2.710 mA cm^{-2}), NiMoO₄ (0.034 mA cm^{-2}), and pure Ni–W–O (0.101 mA cm^{-2}) electrodes and the Pt foil (1.2 mA cm^{-2}). Additionally, electrochemical impedance spectroscopy (EIS) was used to examine the electron transfer process during hydrogen generation (Fig. S10†). The equivalent circuit consisting of a constant phase element, series resistance (R_s) and charge transfer resistance (R_{ct}) is provided in the inset of Fig. S10.† Notably, the smallest values of R_s (0.8 Ω) and R_{ct} (2 Ω) recorded for the Ni–W–O/NiMoO₄-1 electrode substantiated the ease of electron transfer and hence the enhanced kinetics of catalysis across the entire hierarchical heterostructure as compared to those of the other samples. We then evaluated the electrochemical stability of the Ni–W–O/NiMoO₄ heterostructure to assess the robustness of the electrode. To do this, the electrode was subjected to an accelerated degradation test of 5000 continuous cyclic voltammetry (CV) cycles, and the linear sweep voltammetry (LSV) curves were compared before and after the test. It can be seen (Fig. 3d) that there is only an 8% increment in the potential at a current density of 10 mA cm^{-2}. Moreover, a neg-
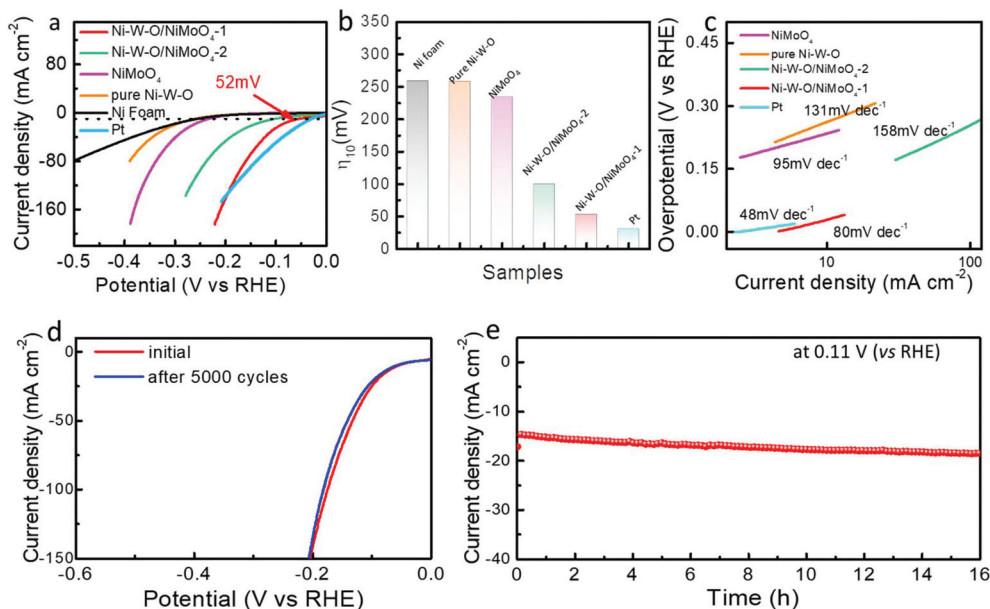

Fig. 3 Electrochemical activity for HER in 1.0 M KOH: (a) HER polarization curve at a scan rate of 5 mV s^{-1} for various electrodes. (b) Comparison of the corresponding η_{10} values collected based on the polarization curves in (a) for various electrodes. (c) Tafel plots obtained from the corresponding polarization curves in (a). (d) Comparison of polarization curves before and after 5000 CV cycles. (e) Chronoamperometry testing of the Ni–W–O/NiMoO₄-1 electrode at 0.11 V (vs. RHE).
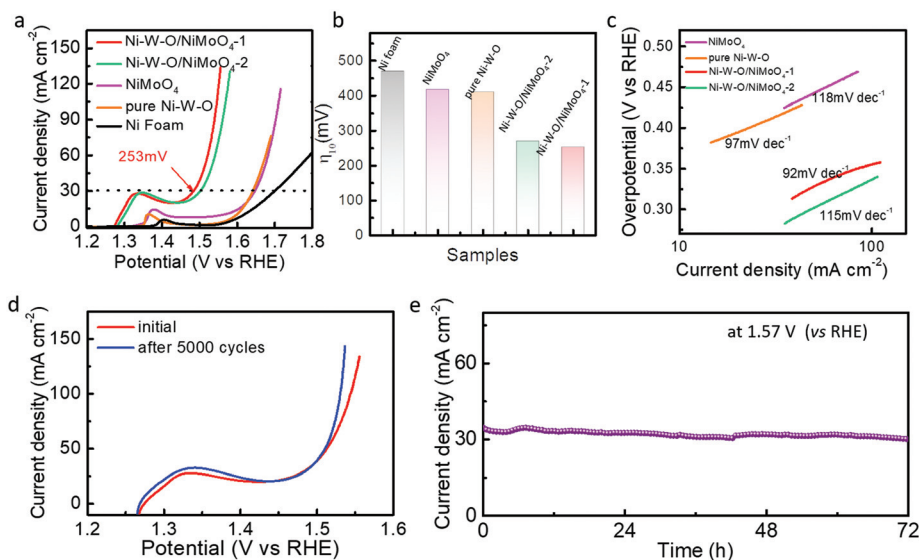
Fig. 4 Electrochemical activity in an O_2-saturated 1.0 M KOH solution for OER. (a) OER polarization curves at a scan rate of 5 mV s^{-1}. (b) Comparison of η_{30} collected based on polarization curves in (a) for various electrodes. (c) Tafel plots for the Ni–W–O/NiMoO$_4$-1 heterostructure and other samples in alkaline media. (d) Comparison of the polarization curves before and after 5000 CV cycles. (e) Chronoamperometry response at 1.57 V (vs. RHE) for the Ni–W–O/NiMoO$_4$-1 electrode for 3 days.

ligible decay can be noticed from the chronoamperometric test (Fig. 3e) during the continuous generation of H_2 gas. This further corroborated the durability of our material in prolonged activities.

In addition to the observed superb HER performance, we found that this Ni–W–O/NiMoO$_4$ heterostructure is also highly active toward electrocatalytic OER in the same electrolyte (1.0 M KOH) saturated with pure O_2 gas (99.99%). The polarization curves of various electrodes in Fig. 4a show a feature such that the oxidation peak appears at around 1.4 V, which is ascribed to the oxidation of Ni^{2+} to Ni^{3+}.[24,27] The overpotentials at the current density of 30 mA cm^{-2} (η_{30}) were obtained to evaluate the OER performances of the Ni–W–O/NiMoO$_4$-1 and other electrodes (Fig. 4b). It was evident that pure NiMoO$_4$ and Ni–W–O are inferior electrocatalysts for OER with large overpotentials of 418 and 410 mV at 30 mA cm^{-2}, respectively. Notably, the Ni–W–O/NiMoO$_4$-1 electrode showed remarkable OER activity with η_{30} of only 253 mV, outperforming most of the previously reported electrocatalysts (Table S2†) such as commercial IrO$_2$ (281 mV at 10 mA cm^{-2}), CoV-UAH (250 mV at 10 mA cm^{-2}),[28] (Co$_4$Mn$_1$)Se$_2$ (274 mV at 10 mA cm^{-2}),[29] and NG-NiFe/MoC$_2$ (320 mV at 10 mA cm^{-2}).[30] It is noteworthy that the Ni–W–O/NiMoO$_4$-2 electrode demonstrated reasonable OER activity with η_{30} of 270 mV. Meanwhile, the Tafel slope of Ni–W–O/NiMoO$_4$-1 was around 92 mV dec^{-1}, substantiating its favourable electrode kinetics for OER. From the EIS spectra (Fig. S11†), we observed small R_{ct} (1.7 Ω) and R_s (0.9 Ω) for the Ni–W–O/NiMoO$_4$-1 electrode at a potential of 0.64 V. In contrast, the NiMoO$_4$ electrode showed large R_{ct}. This might be associated with the fact that the effective improvement in the electronic interaction between Ni–W–O and NiMoO$_4$ endowed this heterostructure with an accelerated charge transfer

process. The synergistic effect from the hierarchical heterostructure formation is therefore crucial for enhanced OER activity in alkaline media. Electrochemical durability is another key index to evaluate the performance of electrocatalysts. Significantly, after 5000 cycling tests (Fig. 4d), the polarization curve is almost identical to the original curve. The long-term electrochemical testing was also probed at a potential of 1.57 V (Fig. 4e), revealing a nearly constant current density after 3 days (72 h) of continuous operation. These results demonstrate the excellent stability of the Ni–W–O/NiMoO$_4$-1 heterostructure in the alkaline electrolyte. After the long-term test, there was no obvious change in the crystal phase and components (Fig. S12–S14†), demonstrating the robust durability of Ni–W–O/NiMoO$_4$-1 during the continuous OER process.

Considering the remarkable HER and OER performances of the Ni–W–O/NiMoO$_4$-1 electrode in 1.0 M KOH, we further used this heterostructure as a cathode and anode simultaneously for overall water splitting in the same solution. Impressively, the cell voltage to afford the current density of 30 mA cm^{-2} was as low as ~1.6 V (Fig. 5a). The inset in Fig. 5a is the optical image of the system, where O_2 and H_2 are released constantly from the surface of the electrodes. Also, its overall water-splitting performance was superior to those of most of the previously reported non-noble metal bifunctional electrodes (Fig. 5b) including Ni$_1$Cr$_1$-LDH,[31] Co$_4$Ni$_1$P NTs,[32] and CoP nanowires[33,34–39] to deliver the same current density (30 mA cm^{-2}). We further tested the long-term durability of our Ni–W–O/NiMoO$_4$-1 electrode at 1.68 V for 30 h (Fig. 5c). The fairly constant current density of 30 mA cm^{-2} elucidated outstanding stability, which is necessary to realize scalability in practical applications.
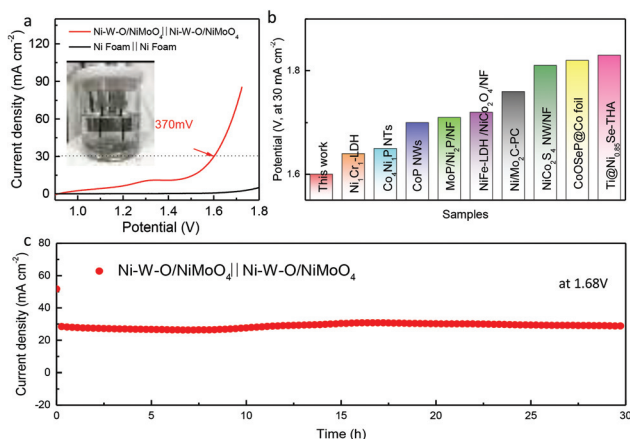
Fig. 5 The overall water splitting performance of the Ni–W–O/NiMoO$_4$-1 heterostructure tested in 1.0 M KOH solution. (a) Polarization curve. (b) Comparison of the overall water splitting cell voltage at a current density of 30 mA cm^{-2} for Ni–W–O/NiMoO$_4$-1 with other bifunctional electrocatalysts. These data were extracted from the published figures in accordance with ref. 31–39. (c) Chronoamperometry response of the Ni–W–O/NiMoO$_4$-1 electrode at 1.68 V.

Conclusions

In conclusion, an Ni–W–O/NiMoO$_4$ heterostructure was successfully synthesized on a porous Ni foam. It could be used as a bifunctional HER and OER electrocatalyst in alkaline media. The presence of Ni–W–O nanosheets on pure NiMoO$_4$ rods, which is crucial for constructing the hierarchical heterostructure, could significantly improve the electrocatalytic activity. A small overpotential (η_{10}) of 52 mV for hydrogen evolution was achieved. Meanwhile, the Ni–W–O/NiMoO$_4$ electrode demonstrated a superior OER performance with an overpotential of 253 mV at a current density of 30 mA cm^{-2} and superb stability after continuous testing for more than 3 days. The effective improvement in the electronic interaction between Ni–W–O and NiMoO$_4$ endowed this heterostructure with outstanding electrochemical activity. Considering the remarkable HER and OER performances in alkaline media, overall water splitting using the Ni–W–O/NiMoO$_4$ heterostructure as an anode and cathode exhibited a cell voltage of 1.60 V at a current density of 30 mA cm^{-2} with outstanding stability. This work paves the way for the future explorations of earth-abundant, binder-free and efficient electrocatalysts for practical overall water splitting.

Experimental methods

Synthesis of NiMoO$_4$ rods

All chemicals were directly used without purification. First, a piece of Ni foam with a size of 2 cm × 3 cm was dipped in 1.0 M HCl for 15 min under ultrasonication, followed by washing several times with deionized water and ethanol. Then, 1.046 g of nickel nitrate hexahydrate (Ni(NO$_3$)$_2$·6H$_2$O, 98%, Alfa Aesar) and 0.176 g of ammonium molybdate (para)hydrate

((NH$_4$)$_6$Mo$_7$O$_{24}$·xH$_2$O, 99.999%, Alfa Aesar) were dissolved in 30 mL deionized water for 1 h with vigorous stirring to form a uniform solution. The clear solution was transferred to a 50 mL Teflon-lined stainless steel autoclave with a Ni foam and then, the reaction was maintained for 6 h at 150 °C. Subsequently, the Teflon-lined stainless steel autoclave was cooled to room temperature and the sample was washed with deionized water and ethanol. Finally, it was dried at 60 °C and annealed at 500 °C in H$_2$/Ar (5 : 95) for 2 h for further measurement.

Synthesis of Ni–W–O/NiMoO$_4$ heterostructure

Typically, 1.0 mmol of nickel chloride hexahydrate (NiCl$_2$·6H$_2$O, Aladdin) and 1.0 mmol of ammonium tungsten oxide hydrate ((NH$_4$)$_{10}$W$_{12}$O$_{41}$·xH$_2$O, Alfa Aesar) were dissolved in 30 mL deionized water. The homogeneous solution was transferred to a 50 mL Teflon-lined stainless steel autoclave and reacted at 130 °C for 8 h. After the reaction, the obtained Ni–W–O/NiMoO$_4$-1 heterostructure was taken out, washed with deionized water and ethanol and then dried at 60 °C for 2 h. Similarly, the Ni–W–O/NiMoO$_4$-2 heterostructure was synthesized using 2 mmol of NiCl$_2$·6H$_2$O and 2 mmol of (NH$_4$)$_{10}$W$_{12}$O$_{41}$·xH$_2$O.

Structural characterization

The morphologies of NiMoO$_4$ rods, Ni–W–O microcubes and Ni–W–O/NiMoO$_4$ heterostructure were characterized via scanning electron microscopy (SEM, Hitachi S-4800 SEM) at 20 kV and transmission electron microscopy (TEM, JEOL JEM-2100F) at 200 kV including the components of the materials. The crystal phase was confirmed by X-ray diffraction (XRD, Bruker D8 Focus) using Cu K$_\alpha$ irradiation (λ = 1.5406 Å). X-ray photoelectron spectroscopy was performed using an ESCALab250 electron spectrometer from Thermo Fisher Scientific Corporation with monochromatic 150 W Al K$_\alpha$ radiation. The pass energy for the narrow scan was 30 eV. The base pressure was about 6.5 × 10^{-10} mbar. The binding energies were referenced to the C 1s line at 284.8 eV from alkyl or adventitious carbon.

Electrochemical measurements

The electrochemical activities of the NiMoO$_4$ rods, Ni–W–O microcubes and Ni–W–O/NiMoO$_4$ heterostructure were studied in an electrochemical station (Princeton Applied Research PARSTAT MC) using a typical three-electrode system. The different electrocatalysts grown on the Ni foam acted as the working electrodes with glassy carbon and Hg/HgO electrode as the counter and reference electrodes, respectively. All the overpotentials were standardized to RHE via the equation $E_{RHE} = E_{Hg/HgO} + 0.098 + 0.059 \times pH$. The electrocatalytic hydrogen evolution measurements were carried out in 1.0 M KOH saturated with N$_2$ for HER, and linear sweep voltammetry (LSV) curves were collected from −0.85 V to −1.5 V at a scan rate of 5 mV s^{-1}. Electrochemical impedance spectroscopy (EIS) in the frequency range from 100 Hz to 0.1 Hz was conducted at −1 V. The stability of the Ni–W–O/NiMoO$_4$ hetero-

structure was exhibited *via* CV with 5000 continuous cycles from −0.9 V to −1.25 V and chronoamperometry under the potential of 0.11 V (*vs.* Hg/HgO electrode) for HER. For the OER measurements, LSV was tested from 0.25 V to 0.9 V (*vs.* RHE) under an O_2-saturated electrolyte. EIS was conducted at 0.64 V (*vs.* Hg/HgO electrode) using the same frequency range. For the stability test, the potential range for CV was from 0.3 V to 0.65 V, and chronoamperometry was carried out at 1.57 V. The exchange current densities of various electrocatalysts were obtained by fitting the linear portion of the Tafel plot at a low cathodic current density, such that the value was calculated according to the Tafel equation. The point at which the abscissa (*i.e.*, current density axis) intersects the extension of the Tafel plot is the value of the exchange current density. During overall water splitting, the Ni–W–O/NiMoO$_4$-1 heterostructure acting as the cathode and the anode simultaneously was investigated in a two-electrode system with the selected potential range from 0.8 V to 1.8 V. Continuous testing at the constant potential of 1.68 V was utilized to evaluate its stability. All the polarization curves were corrected for IR compensation throughout the system to present intrinsic activity.

Conflicts of interest

There are no conflicts to declare.

Acknowledgements

References

1 M. Grätzel, *Nature*, 2001, **414**, 338.
2 F. Wang, T. A. Shifa, X. Zhan, Y. Huang, K. Liu, Z. Cheng, C. Jiang and J. He, *Nanoscale*, 2015, **7**, 19764–19788.
3 N. Cheng, S. Stambula, D. Wang, M. N. Banis, J. Liu, A. Riese, B. Xiao, R. Li, T.-K. Sham, L.-M. Liu, G. A. Botton and X. Sun, *Nat. Commun.*, 2016, **7**, 13638.
4 J. Mahmood, F. Li, S.-M. Jung, M. S. Okyay, I. Ahmad, S.-J. Kim, N. Park, H. Y. Jeong and J.-B. Baek, *Nat. Nanotechnol.*, 2017, **12**, 441.
5 J. Kibsgaard and T. F. Jaramillo, *Angew. Chem., Int. Ed.*, 2014, **53**, 14433–14437.
6 X. Long, G. Li, Z. Wang, H. Zhu, T. Zhang, S. Xiao, W. Guo and S. Yang, *J. Am. Chem. Soc.*, 2015, **137**, 11900–11903.
7 D. Y. Chung, S. W. Jun, G. Yoon, H. Kim, J. M. Yoo, K.-S. Lee, T. Kim, H. Shin, A. K. Sinha, S. G. Kwon, K. Kang, T. Hyeon and Y.-E. Sung, *J. Am. Chem. Soc.*, 2017, **139**, 6669–6674.
8 S. Huang, Y. Meng, S. He, A. Goswami, Q. Wu, J. Li, S. Tong, T. Asefa and M. Wu, *Adv. Funct. Mater.*, 2017, **27**, 1606585.
9 K. Liu, F. Wang, P. He, T. A. Shifa, Z. Wang, Z. Cheng, X. Zhan and J. He, *Adv. Energy Mater.*, 2018, **8**, 1703290.
10 Y. Yang, Z. Lin, S. Gao, J. Su, Z. Lun, G. Xia, J. Chen, R. Zhang and Q. Chen, *ACS Catal.*, 2017, **7**, 469–479.
11 L. Yu, H. Zhou, J. Sun, F. Qin, F. Yu, J. Bao, Y. Yu, S. Chen and Z. Ren, *Energy Environ. Sci.*, 2017, **10**, 1820–1827.
12 Z. Zhang, X. Ma and J. Tang, *J. Mater. Chem. A*, 2018, **6**, 12361–12369.
13 K. Hu, M. Wu, S. Hinokuma, T. Ohto, M. Wakisaka, J.-i. Fujita and Y. Ito, *J. Mater. Chem. A*, 2019, **7**, 2156–2164.
14 Y. Wang, Y. Sun, F. Yan, C. Zhu, P. Gao, X. Zhang and Y. Chen, *J. Mater. Chem. A*, 2018, **6**, 8479–8487.
15 H. Xu, J. Wei, K. Zhang, Y. Shiraishi and Y. Du, *ACS Appl. Mater. Interfaces*, 2018, **10**, 29647–29655.
16 Y. Yang, H. Fei, G. Ruan, C. Xiang and J. M. Tour, *ACS Nano*, 2014, **8**, 9518–9523.
17 S.-H. Bae, J.-E. Kim, H. Randriamahazaka, S.-Y. Moon, J.-Y. Park and I.-K. Oh, *Adv. Energy Mater.*, 2017, **7**, 1601492.
18 S. Yin, W. Tu, Y. Sheng, Y. Du, M. Kraft, A. Borgna and R. Xu, *Adv. Mater.*, 2018, **30**, 1705106.
19 R. Subbaraman, D. Tripkovic, K.-C. Chang, D. Strmcnik, A. P. Paulikas, P. Hirunsit, M. Chan, J. Greeley, V. Stamenkovic and N. M. Markovic, *Nat. Mater.*, 2012, **11**, 550.
20 Z. Li, X. Dou, Y. Zhao and C. Wu, *Inorg. Chem. Front.*, 2016, **3**, 1021–1027.
21 B. Hinnemann, P. G. Moses, J. Bonde, K. P. Jørgensen, J. H. Nielsen, S. Horch, I. Chorkendorff and J. K. Nørskov, *J. Am. Chem. Soc.*, 2005, **127**, 5308–5309.
22 J. Zhang, T. Wang, P. Liu, Z. Liao, S. Liu, X. Zhuang, M. Chen, E. Zschech and X. Feng, *Nat. Commun.*, 2017, **8**, 15437.
23 M. S. Faber, R. Dziedzic, M. A. Lukowski, N. S. Kaiser, Q. Ding and S. Jin, *J. Am. Chem. Soc.*, 2014, **136**, 10053–10061.
24 K. Xiao, L. Xia, G. Liu, S. Wang, L.-X. Ding and H. Wang, *J. Mater. Chem. A*, 2015, **3**, 6128–6135.
25 L. Niu, Z. Li, Y. Xu, J. Sun, W. Hong, X. Liu, J. Wang and S. Yang, *ACS Appl. Mater. Interfaces*, 2013, **5**, 8044–8052.
26 W. He, Z. Liang, K. Ji, Q. Sun, T. Zhai and X. Xu, *Nano Res.*, 2018, **11**, 1415–1425.
27 Z. Y. Yu, C. C. Lang, M. R. Gao, Y. Chen, Q. Q. Fu, Y. Duan and S. H. Yu, *Energy Environ. Sci.*, 2018, **11**, 1890–1897.
28 J. Z. Liu, Y. F. Ji, J. W. Nai, X. G. Niu, Y. Luo, L. Guo and S. H. Yang, *Energy Environ. Sci.*, 2018, **11**, 1736–1741.
29 X. Zhao, X. Li, Y. Yan, Y. Xing, S. Lu, L. Zhao, S. Zhou, Z. Peng and J. Zeng, *Appl. Catal., B*, 2018, **236**, 569–575.
30 Q. Hu, X. Liu, B. Zhu, L. Fan, X. Chai, Q. Zhang, J. Liu, C. He and Z. Lin, *Nano Energy*, 2018, **50**, 212–219.
31 W. Ye, X. Fang, X. Chen and D. Yan, *Nanoscale*, 2018, **10**, 19484–19491.

32 L. Yan, L. Cao, P. Dai, X. Gu, D. Liu, L. Li, Y. Wang and X. Zhao, *Adv. Funct. Mater.*, 2017, **27**, 1703455.

33 W. Li, X. Gao, D. Xiong, F. Xia, J. Liu, W. G. Song, J. Xu, S. M. Thalluri, M. F. Cerqueira, X. Fu and L. Liu, *Chem. Sci.*, 2017, **8**, 2952–2958.

34 C. Du, M. Shang, J. Mao and W. Song, *J. Mater. Chem. A*, 2017, **5**, 15940–15949.

35 Z. Wang, S. Zeng, W. Liu, X. Wang, Q. Li, Z. Zhao and F. Geng, *ACS Appl. Mater. Interfaces*, 2017, **9**, 1488–1495.

36 Z. Y. Yu, Y. Duan, M. R. Gao, C. C. Lang, Y. R. Zheng and S. H. Yu, *Chem. Sci.*, 2017, **8**, 968–973.

37 A. Sivanantham, P. Ganesan and S. Shanmugam, *Adv. Funct. Mater.*, 2016, **26**, 4661–4672.

38 Y.-F. Jiang, C.-Z. Yuan, X. Zhou, Y.-N. Liu, Z.-W. Zhao, S.-J. Zhao and A.-W. Xu, *Electrochim. Acta*, 2018, **292**, 247–255.

39 C. Yang, J. Zhang, G. Gao, D. Liu, R. Liu, R. Fan, S. Gan, Y. Wang and Y. Wang, *ChemSusChem*, 2019, **12**, 1–8.